1 **Study on gene knockout mice and human mutant individual reveals**

2 **absence of CEP78 causes photoreceptor and sperm flagella**

3 **impairments**

4 **Running head:** CEP78 deficiency causes CRD and MMAF

5 Tianyu Zhu,[1,6] Yuxin Zhang,[2,3,6] Xunlun Sheng,[4,6] Xiangzheng Zhang,[1] Yu

6 Chen,[1] Yueshuai Guo,[1] Yaling Qi,[1] Yichen Zhao,[1] Qi Zhou,[1] Xue Chen,[5,†]

7 Xuejiang Guo,[1,†] and Chen Zhao[2,†]

8 [1]State Key Laboratory of Reproductive Medicine, Department of Histology

9 and Embryology, Gusu School, Nanjing Medical University, Nanjing 211166,

10 China; [2]Department of Ophthalmology and Vision Science, Eye & ENT

11 Hospital, Shanghai Medical College, Fudan University, Shanghai 200023,

12 China; [3]Department of Ophthalmology, Children's Hospital of Nanjing Medical

13 University, Nanjing Medical University, Nanjing 210000, China; [4]Department

14 of Ophthalmology, Ningxia Eye Hospital, People Hospital of Ningxia Hui

15 Autonomous Region (First Affiliated Hospital of Northwest University for

16 Nationalities), Yinchuan 750000, China; [5]Department of Ophthalmology, The

17 First Affiliated Hospital of Nanjing Medical University, Nanjing Medical

18 University, Nanjing 210029, China

19 [6]These authors contributed equally to this work.

20 **Correspondence:** Chen Zhao (dr_zhaochen@163.com) or Xuejiang Guo

21 (guo_xuejiang@njmu.edu.cn) or Xue Chen (drcx1990@vip.163.com).

22

23   Abstract

24   Background:

25   Cone-rod dystrophy (CRD) is a genetically inherited retinal disease

26 characterized by photoreceptor degeneration. In some rare cases, CRD and

27 hearing loss can be associated with male fertility, while the underlying

28 mechanism is not well known.

29

30   Methods:

31   Using CRISPR/Cas9 system, we generated $Cep78^{-/-}$ mice. And

32 electroretinogram (ERG), immunofluorescence staining and transmission

33 electron microscopy (TEM) were used to analyze visual function and

34 photoreceptor ciliary structure changes in $Cep78^{-/-}$ mouse. HE/PAS staining,

35 scanning-electron microscopy (SEM) were conducted to $Cep78^{-/-}$ mice and

36 human CRD patient with CEP78 protein loss to illustrate male infertility and

37 multiple morphological abnormalities of the sperm flagella (MMAF) caused

38 by CEP78 deficiency. TEM and immunofluorescence staining were

39 performed to characterize morphological and molecular changes of sperm

40 flagella microtubule arrangement, centriole development and spermatid head

41 shaping in $Cep78^{-/-}$ mice. Mass-spectrometry analyses were conducted to

42 identify protein abnormalities after $Cep78$ deletion and Cep78 interacting

43 proteins in spermiogenesis. Co-immunoprecipitation was used to show the

44 Cep78-Ift20-Ttc21a trimer. The role of Cep78-Ift20-Ttc21a trimer in

45 cilliogenesis and centriole elongation was assessed by cilia induction assay.

46

47   Results:

48    $Cep78$ knockout mice exhibited impaired function and morphology of

49 photoreceptors, typified by reduced electroretinogram amplitudes, disrupted

50 translocation of cone arrestin, attenuated and disorganized photoreceptor

51 outer segments (OS) disks and widen OS bases, as well as interrupted cilia

52 elongations and structures. $Cep78$ deletion also caused male infertility and

53 MMAF, with disordered "9 + 2" structure and triplet microtubules in sperm

54 flagella. CEP78 forms a trimer with intraflagellar transport (IFT) proteins

55 IFT20 and TTC21A essential for sperm flagella formation, is essential for

56 their interaction and stability, and recruits IFT20 to centrosome. Insufficiency

57 of any component in the trimer causes centriole elongation and cilia

58 shortening. Additionally, absence of CEP78 protein in human leaded to

59 similar phenotypes in vision and MMAF as $Cep78^{-/-}$ mice.

60

61 Conclusions:

62 We found *CEP78* as the causative gene of CRD with MMAF in human

63 and mouse. Cep78 forms a trimer with Ift20 and Ttc21a, and regulate the

64 interaction, stability and localization of the trimer proteins, which regulate

65 cilliogenesis, centriole length, and sperm flagella formation.

66

67 Funding:

Introduction

Cone-rod dystrophy (CRD) is a genetically inherited retinal disease characterized by photoreceptor degeneration[1]. Many CRD pathogenic genes are associated with connecting cilia in photoreceptor, a type of non-motile cilia. CRD usually exists with combination of immotile cilia defects in other systems. CEP250 mutation is associated with CRD and hearing loss [2]; mutations in CNGB1 cause CRD and anosmia [3]; and CEP19 mutation leads to CRD with obesity and renal malformation[4]. Different from photoreceptor connecting cilia, sperm flagellum is motile cilia. Motile and immotile cilia defects usually do not occur at the same time. However, occasionally, CRD can also occur as a syndrome in combination of abnormalities of sperm flagella. As this syndrome leads to defects of two unrelated physiological functions, vision and reproduction, comprehensive analysis of its specific genetic etiology and molecular mechanism is still limited.

Centrosomal protein of 78 kDa (CEP78), protein encoded by the *CEP78* gene (MIM: 617110), is a centriolar protein composed of 722 amino acids and possesses two leucine-rich repeats and a coiled-coil domain[5]. CEP78 localizes to the distal region of mature centrioles and is exclusively expressed in ciliated organisms, supporting its crucial function in maintaining centrosome homeostasis[6, 7]. Mutations in the *CEP78* gene cause autosomal recessive CRD and hearing loss (CRDHL; MIM: 617236)[8-12].

4

97   Deregulation of Cep78 is also associated with colorectal cancer[13], prostate

98   cancer[14], and asthenoteratozoospermia[12]. As a centrosomal protein,

99   CEP78 functions downstream of CEP350 to control biogenesis of primary

100   cilia [15], and regulates centrosome homeostasis through interactions with

101   other centrosomal proteins, including CEP76, CP110 and EDD-DYRK2-

102   DDB1^{VprBP}[6]. Despite these findings, the biological function of Cep78,

103   especially its function and mechanism in CRD with male infertility remains to

104   be elucidated.

105   In this study, based on results of a male patient carrying *CEP78*

106   mutation and *Cep78* gene knockout mice, we report CEP78 as a new

107   causative gene for a distinct syndrome involving two phenotypes, CRD and

108   male sterility[16]. We revealed that CEP78 deficiency caused dysfunction

109   and irregular ciliary structure of photoreceptors. Deletion of Cep78 triggered

110   male infertility, spermatogenesis defects, aberrant sperm flagella structures

111   and manchette formation, and abnormal spermatid centriole length in male

112   mice. The male patient carrying homozygous *CEP78* mutation leading to

113   CEP78 protein loss also presented syndromic phenotypes including CRD,

114   hearing loss, and multiple morphological abnormalities of the sperm flagella

115   (MMAF). IFT20 and TTC21A are both IFT proteins have interaction with each

116   other and vital for spermatogenesis and cilliogenesis[17]. CEP78 forms a

117   trimer with IFT20 and TTC21A, which are vital for spermatogenesis and

118   cilliogenesis[17-19], and regulated their interaction and stability. CEP78

5

119   recruits centrosome localization of IFT20. Defects of CEP78 trimer leaded to

120   extended centriole and cilia shortening.

121

Results

Generation of *Cep78*^{-/-} mice

To investigate the role of CEP78, we generated *Cep78* knockout mice using clustered regularly interspaced short palindromic repeats (CRISPR)/Cas 9 system. A sgRNA targeting exons 2 and 11 of the *Cep78* mice gene (**Supplementary Figure S1A**) was designed, generated, and injected into C57BL/6 mice zygote with the Cas 9 RNA. Genotyping confirmed deletion of exons 2 to 11 in heterozygotes and homozygotes (**Supplementary Figure S1B**). As revealed by immunoblotting, expression of Cep78 protein was completely absent in the neural retina and testes of *Cep78*^{-/-} mice (**Supplementary Figures S1C-D**), suggesting successful generation of *Cep78* knockout mice.

Cep78^{-/-} mice show photoreceptor impairments

To reveal the retinal phenotypes associated with Cep78 deletion, we studied the functional and morphological changes in *Cep78*^{-/-} mice retina. We initially used electroretinogram (ERG) to detect visual functions of *Cep78*^{-/-} mice. ERG results of *Cep78*^{-/-} mice and their heterozygous littermates at ages of 3-, 6-, 9- and 18-month were recorded. Scotopic a- and b-wave, together with photopic b-wave amplitudes were reduced in *Cep78*^{-/-} mice when compared to age-matched *Cep78*^{+/-} mice (**Figures 1A-E**). The reduction extended as age increased. According to our data, amplitudes of

7

144   scotopic a-wave showed approximately 13.6%, 39.1%, 40.8%, and 64.8%

145   decrease in $Cep78^{-/-}$ mice at 3-, 6-, 9- and 18-month respectively (**Figures**

146   **1A, C**), and amplitudes of scotopic b-wave were down-regulated by 19.9%,

147   30.5%, 35.6%, and 58.3% in $Cep78^{-/-}$ mice at 3-, 6-, 9- and 18-month

148   respectively (**Figures 1A**, **D**). Similarly, amplitudes of photopic b-wave were

149   decreased by 39.4%, 39.8%, 52.8%, and 69.0% in $Cep78^{-/-}$ mice at 3-, 6-, 9-

150   and 18-month respectively (**Figures 1B, E**).

151   In normal retina, light exposure drives rapid movement of cone arrestin

152   into outer segments (OS) of cone photoreceptors[20]. Herein, we tested

153   whether Cep78 knockout would disrupt such translocation of cone arrestin in

154   cone photoreceptors. Immunostaining patterns of cone arrestin in dark- and

155   light-adapted $Cep78^{+/-}$ and $Cep78^{-/-}$ mice retinas were compared. In dark-

156   adapted retina, cone arrestin was localized in the synaptic region, outer

157   nuclear layer (ONL), and outer and inner segments. No difference was

158   observed in distribution patterns of cone arrestin between $Cep78^{+/-}$ and

159    $Cep78^{-/-}$ mice (**Figure 1F**). Light exposure of 2 hours triggered a shift of cone

160   arrestin from the inner cellular compartments to the OS in both $Cep78^{+/-}$ and

161    $Cep78^{-/-}$ mice. However, light-induced translocation of cone arrestin in

162    $Cep78^{-/-}$ mice retina was slower and more limited than in $Cep78^{+/-}$ mice

163   (**Figure 1F**). Thus, above data suggested that regular functions of retina

164   were disturbed in $Cep78^{-/-}$ mice.

165   We next investigated morphological changes in retina of $Cep78^{-/-}$ mice.

8

166   Spectral domain-optical coherence tomography system (SD-OCT) was

167   applied to visualize all layers of mice retina. SD-OCT showed that

168   thicknesses of ONL were attenuated in $Cep78^{-/-}$ mice when compared to

169    $Cep78^{+/-}$ mice at ages of 3-, 9-, and 12-month (**Figures 1G-J**). The

170   attenuation became more evident along with increasing of age (**Figures 1G-**

171   **J**). We also utilized transmission electron microscopy (TEM) to observe the

172   ultra-structure of photoreceptors. As evidenced by TEM, photoreceptor OS

173   are regularly lined and shaped in $Cep78^{+/-}$ mice at 3-, 6-, and 9-month age.

174   However, disorganized, sparse, and caduceus photoreceptor OS disks, and

175   widen OS bases were observed in age-matched $Cep78^{-/-}$ mice (**Figure 1K**).

176   Collectively, our results indicated that both functions and morphologies of

177   mice photoreceptor were disturbed upon Cep78 deletion.

178

179   ***Cep78*$^{-/-}$ mice exhibit disturbed ciliary structures in photoreceptors**

180   Since CEP78 is a ciliary protein and *CEP78* mutation was found

181   associated with primary-cilia defects[9], we then aimed to analyze whether

182   *CEP78*$^{-/-}$ mice exhibit abnormal ciliary structure using immunofluorescence

183   staining and TEM. Ciliary axonemes and basal bodies were labeled with

184   antibody against Ac-α-tubulin in immunofluorescence staining. Our data

185   indicated that cilia were shortened in $Cep78^{-/-}$ mice at 3-, 6-, and 9-month

186   age compared to age-matched $Cep78^{+/-}$ mice (**Figure 2A**). We further used

187   TEM to visualize longitudinal sections of the ciliary region of photoreceptors.

9

188   Based on our findings, photoreceptors of $Cep78^{-/-}$ mice had shortened

189   connecting cilia with their microtubules spread in their upper part (**Figures**

190   **2B-F**). Structures of basal bodies, adjacent daughter centrioles, or other

191   organelles of inner segment were not altered in $Cep78^{-/-}$ mice (**Figures 2D-**

192   **F**). Thus, our data suggested that Cep78 deficiency interrupts cilia elongation

193   and disturbed ciliary structures in photoreceptors.

194

195   **Cep78 deletion leads to male infertility and MMAF in mice**

196   Unexpectedly, we found that $Cep78^{-/-}$ male mice were infertile during the

197   breeding of $Cep78^{-/-}$ mice. We thus explored the reproductive functions of

198    $Cep78^{-/-}$ male mice. No difference was revealed between the testis weight,

199   body weight, and testis/body weight of $Cep78^{+/-}$ and $Cep78^{-/-}$ male mice

200   (**Supplementary Figures S2A-C**). Mating test with $Cep78^{+/-}$ female mice for

201   3 months showed that $Cep78^{-/-}$ male mice were infertile (**Figure 3A**). To

202   further explore the underlying causes for male infertility of $Cep78^{-/-}$ mice, we

203   assessed the concentration, motility and progressive motility of sperm

204   isolated from cauda epididymis using computer-assisted sperm analysis

205   (CASA), and all three parameters were decreased upon $Cep78$ deletion

206   (**Supplementary Table S1** and **Supplementary Movies 1-2**). Consistently,

207   hematoxylin-eosin (H&E) staining also showed less spermatozoa in both

208   caput and cauda epididymis of $Cep78^{-/-}$ male mice compared with age

209   matched $Cep78^{+/-}$ male mice (**Figure 3B**).

10

210   Multiple abnormalities of sperm head and flagella in *Cep78*$^{-/-}$ male mice

211   were initially detected by light microscopy (**Figures 3C-D**) and scanning-

212   electron microscopy (SEM; **Figures 3E-I**), which identified severely distorted

213   sperm heads and flagella (**Figures 3D, F-I**), including absent (**Figures 3D,**

214   **F**), short (**Figures 3D, G**), coiled (**Figures 3D, H**), and multi-flagella (**Figure**

215   **3I**). Spermatozoa with abnormal heads, necks and flagella accounted for

216   92.10%, 82.61% and 95.67% of total spermatozoa respectively in *Cep78*$^{-/-}$

217   male mice (**Supplementary Table S1**). Immunofluorescence staining was

218   also used to study sperm morphology, results of which were consistent with

219   those of light microscopy and SEM. Sperm axoneme was stained using

220   antibody against Ac-α-tubulin, and short flagella were frequently observed

221   (**Figures 3J-M**).

222   We next applied quantitative mass spectrometry (MS) on elongating

223   spermatids lysates of *Cep78*$^{+/-}$ and *Cep78*$^{-/-}$ mice to reveal effects of Cep78

224   insufficiency on testicular protein expressions and pathway regulations. We

225   set the threshold as a fold-change greater than 1.5 and p value less than

226   0.05, and identified a total of 806 down-regulated proteins and 80 up-

227   regulated proteins upon Cep78 depletion, which were visualized using

228   hierarchical clustering analyses (**Figure 3N** and **Supplementary Table S2**).

229   Consistent to above findings in morphological anomalies in sperm,

230   significantly enriched gene ontology (GO) terms in cellular components

231   included sperm principal piece, sperm fibrous sheath, acrosomal vesicle,

232   motile cilium, centrosome, microtubule skeleton and dynein complex (**Figure**

233   **3O** and **Supplementary Table S3**). Taken together, Cep78 deletion leaded

234   to decreased count, motility and progressive motility of sperm, morphological

235   abnormalities of sperm head and flagella in mice, as well as dysregulated

236   sperm proteins thus accounting for male infertility.

237

238   **Defective microtubule arrangements and elongated centrioles in sperm**

239   **flagella of *Cep78$^{-/-}$* mice**

240   To determine which spermatogenesis stage that Cep78 affected on, we

241   compared histology of testicular tissue sections between *Cep78$^{-/-}$* and

242   *Cep78$^{+/-}$* male mice using periodic acid-Schiff (PAS) staining. Light

243   microscopy showed an apparent scarcity of sperm flagella visible in the

244   lumens of *Cep78$^{-/-}$* testes (**Figures 4A-B**), with flagellar formation defects

245   observed from stages I-III till stages VII-VIII during spermatogenesis

246   (**Figures 4B**), suggesting that Cep78 was involved at the stage of sperm

247   flagellar formation. Very few spermatids reached maturity successfully and

248   passed into epididymis (**Supplementary Table S1**).

249   To further carefully characterize *Cep78$^{-/-}$* mice phenotype, we analyzed

250   the ultra-structure of mouse testes using TEM. Based on our findings,

251   *Cep78$^{+/-}$* sperm showed well aligned arrangements of connecting segments,

252   axoneme microtubules, mitochondria, outer dense fibers (ODF), and fiber

253   sheaths in longitudinal section of neck, middle, and principal pieces (**Figures**

254   **4C-D**). However, disordered mitochondria and a jumble of unassembled

255   flagellar components were presented in *Cep78*$^{-/-}$ sperm (**Figures 4E-F**). In

256   cross sections of middle and principal regions, *Cep78*$^{+/-}$ sperm exhibited

257   well-aligned ODF and typical "9+2" arrangement of microtubules, which were

258   typified by 9 peripheral microtubule doublets surrounding a central pair of

259   singlet microtubules (**Figures 4G-H**). In contrast, *Cep78*$^{-/-}$ sperm showed

260   complete derangement of ODF and scattered "9+2" microtubules (**Figures**

261   **4I-J**). In normal sperm flagella, distal centriole develops an atypical centriole

262   structure, whose microtubules are doublets instead of triplets. Triplet

263   microtubules can only be observed at proximal centrioles[21]. In *Cep78*$^{-/-}$

264   sperm, triplet microtubules, which were supposed to exist only in proximal

265   centrioles, were found at both middle and principal pieces of sperm flagella

266   (**Figures 4I-J**), indicating abnormal elongation of centrioles during sperm

267   flagella formation.

268   Tubules in axoneme are formed from centrosome. The various types of

269   aberrant sperm flagella observed in mice with CEP78 defects, together with

270   the triplet microtubules found in principal and middle pieces of sperm flagella

271   upon CEP78 deletion, suggested centriole anomalies as potential causes for

272   deregulation of sperm development in mouse. Previous *in vitro* studies

273   showed that interference of Cep78 leaded to elongation of centriole[6]. To

274   further elucidate whether Cep78 regulates centriole length in

275   spermiogenesis, we stained centrioles and peri-centriole materials with anti-

13

276   centrin 1 and γ-tubulin, respectively. Two-dot staining pattern of disengaged

277   centrioles was observed in *Cep78*$^{+/-}$ spermatids (**Figure 4K**), while depletion

278   of Cep78 promoted centriole elongation in spermatids (**Figure 4K**),

279   supporting the role of Cep78 in regulating centriole structures and functions.

280   Collectively, our data revealed defective microtubule arrangements and

281   elongated centrioles in sperm flagella of *Cep78*$^{+/-}$ mice.

282

283   ***Cep78*$^{-/-}$ testes present abnormalities in spermatid head formation**

284   **during spermiogenesis**

285   In addition to axonemal defects in sperm flagella, *Cep78*$^{-/-}$ testes also

286   exhibit deformation of spermatid nuclei, which was presented by abnormal

287   club-shaped nuclear morphology of elongated spermatids since step 10, in

288   contrast to the normal hook-shaped head in *Cep78*$^{+/-}$ elongated spermatids

289   (**Figures 4B, 5A**). Abnormal elongation of manchette structures in testicular

290   spermatids of *Cep78*$^{-/-}$ mice during spermiogenesis was also shown by

291   immunofluorescence staining (**Figure 5B**), which supported above findings

292   by PAS staining.

293   Further analyses with TEM observed various ultra-structural defects in

294   sperm head formation of *Cep78*$^{-/-}$ spermatids. As indicated by TEM, *Cep78*$^{+/-}$

295   spermatids underwent a series of dramatic changes and presented regular

296   reshaping of sperm head, including nuclear condensing, manchette

297   formation, and acrosomal biogenesis (**Figures 5C**, **G, J**). TEM suggested

298   that nuclear condensing was normal in $Cep78^{-/-}$ spermatids (**Figures 5D-F,**

299   **H-I, K-M**). Similar expressional intensity and localization of transition protein

300   1 from stage IX of spermatogenesis to stage I-III in $Cep78^{+/-}$ and $Cep78^{-/-}$

301   mice were revealed by immunofluorescence staining, confirming the TEM

302   data and suggesting that nuclear condensation was not affected upon Cep78

303   deletion (**Figure 5N**). We also performed spermatocyte spreading of $Cep78^{+/-}$

304   and $Cep78^{-/-}$ mice testicular tissues to detect ratios of spermatocytes at

305   leptotene, zygotene, pachytene, and diplotene stages. Based on our results,

306   Cep78 loss showed no effects on spermatocyte development at all four

307   stages (**Figures 5O-P**), implying that Cep78 deletion did not affect the

308   prophase of meiosis I.

309   The manchette structure, consisted of a series of parallel microtubule

310   bundles that extended from perinuclear rings of nucleus to distal cytoplasm

311   and are closely proximity to or parallel to nuclear membranes, regulates

312   sperm head formation during spermiogenesis[22]. We herein revealed

313   various abnormalities in manchette formation and acrosomal biogenesis in

314    $Cep78^{-/-}$ spermatids, including an abnormal nuclear constriction at the site of

315   perinuclear rings (**Figure 5D**), ectopic and asymmetric perinuclear rings

316   together with disordered manchette microtubules (**Figures 5E-F, H-I, K**),

317   abnormal acrosome and nuclei invagination (**Figure 5L**), and detached

318   acrosome from nuclear membrane (**Figure 5M**). The defective spermatid

319   manchette formation in $Cep78^{-/-}$ mice led to peculiar shaping of nucleus and

15

320   abnormal sperm head formation. Therefore, the above findings indicated that

321   absence of Cep78 generates defective spermatid head formation.

322

323   *CEP78* **mutation causes male infertility and MMAF in human patient**

324   **with CRD**

325   We have previously linked the *CEP78* c.1629-2A>G mutation with

326   autosomal recessive CRDHL, and revealed a 10 bp deletion of *CEP78* exon

327   14 in mRNA extracted from white blood cells of patient carrying *CEP78*

328   c.1629-2A>G mutation[8]. We further explored whether this mutation will

329   disturb CEP78 protein expression using immunoblotting. Blood sample was

330   collected from this patient and an unaffected control for protein extraction.

331   Our results revealed absence of CEP78 protein in white blood cells of patient

332   carrying *CEP78* c.1629-2A>G mutation (**Supplementary Figure S3**),

333   suggesting that this mutation leads to loss of CEP78 protein.

334   Since Cep78 deprivation led to male infertility and sperm flagellar

335   defects in mice, and *CEP78* c.1629-2A>G mutation caused degradation of

336   CEP78 protein in human, we thus investigated reproductive phenotype of the

337   previously reported male patient, who carried homozygous *CEP78* c.1629-

338   2A>G mutation and was diagnosed with CRD and hearing loss[23]. The

339   patient is infertile. His semen volume was 2.6 mL, which was among the

340   normal range (**Supplementary Table S1**). However, CASA revealed obvious

341   reductions in sperm concentration, motility, and progressive motility in the

16

342   *CEP78*-mutated man according to standard of the World Health Organization

343   (WHO) guidelines (**Supplementary Table S1**). In addition, impaired sperm

344   movement of the patient is presented in **Supplementary Movies 3**.

345   Patient's semen sample was further submitted for morphological

346   analyses using light microscopy and SEM, both of which showed typical

347   MMAF phenotypes, such as abnormal heads (95.42%), necks (85.62%) and

348   flagella (97.39%) (**Figures 6A-J** and **Supplementary Table S1**). A great

349   diversity of abnormal flagella was observed including short flagella (**Figures**

350   **6B, G**), coiled flagella (**Figures 6C, I**), absent flagella (**Figures 6D, H**), and

351   multi flagella (**Figures 6E, J**). The patient's sperm also had a series of sperm

352   head abnormalities, such as large acrosome area (**Figure 6B**), pear shaped

353   nucleus (**Figure 6C**), conical nucleus (**Figure 6D**), and excessive acrosome

354   vacuoles (**Figure 6E**). TEM was further applied to visualize the ultra-

355   structures of spermatozoa in the male patient carrying *CEP78* c.1629-2A>G

356   mutation. Based on our data, multiple ultra-structural abnormalities were

357   observed in the spermatozoa of case as compared to those of age matched

358   healthy male individual (**Figures 6K-R**). For example, longitudinal sections

359   showed disordered arrangements of mitochondrial sheaths, severe

360   axonemal disorganization, and fibrous sheath hyperplasia (**Figures 6L, N**).

361   Instead of the typical "9+2" microtubule structure in exoneme of normal

362   sperm flagella (**Figures 6O, Q**), absent or reduced central-pair microtubules

363   and disarranged peripheral microtubule doublets were frequently observed in

17

364 cross sections (**Figures 6P, R**). Similar to the *Cep78*$^{-/-}$ mice data, triplet

365 microtubules unique to proximal centrioles in sperm were also observed in

366 both principal and middle pieces of patient's sperm flagella (**Figures 6P, R**).

367 Taken together, this patient carrying *CEP78* c.1629-2A>G mutation

368 presented typical MMAF phenotypes.

369

370 **CEP78 forms a trimer with IFT20 and TTC21A, and is essential for their**

371 **interaction and stability to regulate centriole and cilia lengths**

372 To reveal the interaction between CEP78 and other proteins during

373 spermiogenesis, we performed anti-Cep78 immunoprecipitation (IP) coupled

374 with quantitative MS (IP-MS) on testicular lysates of *Cep78*$^{+/-}$ and *Cep78*$^{-/-}$

375 mice. A total of 16 ciliary proteins were initially screened out by proteomic

376 analyses (**Supplementary Table S4**), among which Ift20 and Ttc21A were

377 essential for sperm flagella assembly and male fertility. These two proteins

378 bound together as a dimer and loss of IFT20 or TTC21A was found to cause

379 male infertility and MMAF phenotypes[17, 19], we thus hypothesized that

380 CEP78 regulates human and mice phenotypes by interacting with IFT20 and

381 TTC21A as a tri-mer. To explore this hypothesis, we first tested whether the

382 three proteins directly bind with each other using co-immunoprecipitation (co-

383 IP) and immunoblotting analyses in HEK293T cells overexpressing tagged

384 proteins. Direct interactions between CEP78 and IFT20 (**Figure 7A**), CEP78

385 and TTC21A (**Figure 7B**), and IFT20 and TTC21A (**Figure 7C**) were

18

386   identified, supporting our hypothesis.

387   We next detected whether Cep78 depletion would cause instability of

388   the protein complex and disturbs its functions. As revealed by co-IP and

389   immunoblotting results, the direct binding between Ift20 and Ttc21a was

390   severely disrupted upon Cep78 knocking out (**Figure 7D**), indicating that

391   Cep78 is essential for maintaining stability of the tri-mer. We also found that

392   expressions of both Ift20 and Ttc21a were decreased in testes of *Cep78*$^{-/-}$

393   mice compared to *Cep78*$^{+/-}$ mice (**Figures 7E, F, G**), suggesting that

394   disruption of the trimer potentially affected stability of all components.

395   Decreased Ift20 expression was also detected by immunofluorescence

396   staining in 3T3 cells transfected with Cep78-siRNA compared to cells

397   transfected with scramble siRNA (**Figure 7H**). Quantitative real-time PCR (Q-

398   PCR) identified that expressions of Cep78 was remarkably knocked down to

399   15% by Cep78-siRNA in 3T3 cells (**Supplementary Figure S4A**). In

400   addition, the co-localization between Ift20 and centrioles in 3T3 cells

401   transfected with scramble siRNA was altered upon Cep78 knocking down

402   (**Figure 7H**), supporting that Cep78 insufficiency might disturb the regular

403   functions of Ift20.

404   We then aimed to determine the function of this tri-mer. We found that all

405   three components of the trimer located in the base of the cilium of 3T3 cells

406   (**Figure 7I**), indicating its role in regulating ciliogenesis. Ciliary axonemes

407   and centrioles were labeled with antibodies to Ac-α-tubulin and γ-tubulin

19

408   respectively. We found that cilium length was reduced in 3T3 cells

409   transfected with Cep78-siRNA, Ift20-siRNA or Ttc21a-siRNA compared to

410   cells transfected with scramble siRNA (**Figures 7J-K**). Efficiencies for Ift20

411   and Ttc21a knocking down using Ift20-siRNA and Ttc21a-siRNA in 3T3 cells

412   were confirmed by Q-PCR (**Supplementary Figures S4B-C**). However,

413   centrioles were elongated in 3T3 cells with Cep78 or Ift20 knocking down,

414   but not in cells with insufficient Ttc21a (**Figures 7L-M**). Thus, our data

415   suggested that insufficiency of any component in the trimer causes cilia

416   shortening and centriole elongation, which was consistent with phenotypes

417   we observed in *Cep78$^{-/-}$* mice. Collectively, our findings suggested that

418   CEP78 directly interacts with IFT20 and TTC21A to regulate axonemal and

419   centrosomal functions.

20

Discussion

420

421   In our study, we found *CEP78* as the causal gene of CRD with male

422   infertility and multiple morphological abnormalities of the sperm flagella using

423   *Cep78*^{-/-} mouse. Cep78 forms a trimer with IFT20 and TTC21A (**Figure 8**),

424   which are essential for sperm flagella formation[17, 19]. Cep78 is important

425   for the interaction and stability of the trimer proteins, which regulate

426   cilliogenesis. Absence of CEP78 protein also leaded to CRD and multiple

427   morphological abnormalities of the sperm flagella in human.

428   CEP78 belongs to the centrosomal and ciliary protein family, mutations

429   in other centrosomal genes, such as CEP19, CEP164, CEP250 and

430   CEP290, could disrupt ciliary assembly and generate retinopathy[2, 4, 24-

431   27]. However, there's no evidence that loss of the above centrosomal

432   proteins can simultaneously cause CRD and male infertility. While in this

433   study, we provide evideces that CEP78 is a causal gene of CRD and male

434   infertility. Absence of Cep78 in human and mouse both present the same

435   phenotypes of CRD, and multiple morphological abnormalities of the sperm

436   flagella.

437   In *Cep78*^{-/-} photoreceptors, we observe shortened connecting cilia,

438   spreading of microtubule doublets in the proximal half, and aberrant

439   organizations of outer segment disks, which is similar to previous findings in

440   mice with disrupted Fam161a protein[28]. Our data provide *in vivo* evidence

441   for CEP78's role in maintaining structures and functions of microtubule

21

442   doublets in the connecting cilium of photoreceptors.

443   Despite of abnormal arrangement of sperm flagella microtubule, we here

444   find that CEP78 disruption could cause abnormal formation of manchette, a

445   transient structure surrounding the elongating spermatid head and is only

446   present during spermatid elongation[22, 29]. During spermiogenesis,

447   manchette and sperm tail axoneme are two microtubular-based platforms

448   that deliver cargo proteins to sperm heads and tails, respectively[29]. How

449   manchette is formed is still not fully elucidated. The majority views hold that

450   manchette microtubules are nucleated at spermatid centrosomes[29, 30],

451   which start from nucleator γ-tubulin of the centrosomal adjunct and end at

452   perinuclear rings[31, 32]. According to our data, other than disorganized

453   manchette structures, elongated centrioles are also observed in $Cep78^{-/-}$

454   mice, indicating CEP78's potential role in organizing manchette

455   microtubules. Taken together, CEP78 dysfunction specifically impairs

456   organization of microtubular-based structures.

457   Previous study indicated the involvement of CEP78 in regulation of

458   centriole length. We herein also observed stretched centriole length in

459   $Cep78^{-/-}$ spermatids, and down-regulation of the interacting protein of

460   CEP78, Ift20. CEP78 can recruit the centriole localization of Ift20, whose

461   knock-down causes centriole elongation. Moreover, triplet microtubules,

462   which are specific to proximal centriole in sperm[21], are aberrantly found in

463   principal and middle pieces of sperm flagella from both the male patient with

22

464   *CEP78* mutation and *Cep78*$^{-/-}$ mice, possibly caused by abnormal elongation

465   of the triplet microtubules of centriole. However, such anomaly in both human

466   and mouse sperm has never been reported before.

467   We found that CEP78 loss leaded to shortening of sperm flagellum, with

468   Cp110 down-regulated in *Cep78*$^{-/-}$ testis (**Supplementary Figure S5**), which

469   is inconsistent with Gonçalves et al.'s findings that cells lacking CEP78

470   display up-regulated CP110 and reduced cilia frequency with long cilia

471   phenotype[15]. It seems that Cep78 may regulate formation of sperm

472   flagellum by a different mechanism. Our analysis of interacting proteins of

473   Cep78 showed that CEP78 forms a trimer with two other proteins required

474   for sperm flagellar formation, IFT20 and TTC21A. Cep78 regulates the

475   interaction between Ift20 and Ttc21a, and loss of Cep78 leaded to

476   downregulation of the other two components of the trimer. Insufficiency of

477   any component in the trimer disrupts its structure and affects stability of all

478   components, leading to cilia shortening. IFT20, belonging to the IFT family, is

479   essential for assembly and maintenance of cilia and flagella[33]. It is required

480   for opsin trafficking and photoreceptor outer segment development[18], and

481   plays important roles in spermatogenesis and particularly spermiogenesis by

482   transferring cargo proteins for sperm flagella formation[33]. During

483   spermiogenesis, IFT20 is transported along the manchette microtubules[34].

484   IFT20 is essential to male fertility, spermatogenesis and particularly

485   spermiogenesis by transferring cargo proteins for sperm flagella formation.

23

486   Multiple sperm flagella abnormalities are observed in *Ift20* mutant mice,

487   including short and kinked tail[19]. TTC21A/IFT139 is also essential for

488   sperm flagellar formation[17]. TTC21A directly interacts with IFT20, and

489   mutations in *TTC21A* gene are reported to cause MMAF in both human and

490   mice[17]. However, more studies are still warranted to better elucidate the

491   biological mechanism of CEP78 in regulating features of spermatozoa and

492   photoreceptors.

493   CEP78 protein is highly conserved among vertebrate organism with

494   human and mouse CEP78 proteins sharing over 80% similarity. Disease

495   phenotypes and changes of ultra-structures were highly-consistent between

496   human and mice upon CEP78 depletion. Our study also reveals *Cep78*$^{-/-}$

497   mice model as an applicable animal model for therapeutic research of such

498   distinct syndrome.

499   In conclusion, we identify CEP78 as a causative gene for a type of

500   syndrome involving CRD and male infertility. CEP78 dysfunction induces

501   similar phenotypes and ultra-structure changes in human and mice, including

502   disturbed ciliary structure in photoreceptors, defective sperm flagella

503   structures, and aberrant spermatid head formation. We also found that

504   CEP78 formed a trimer with ciliary proteins IFT20 and TTC21A, and

505   regulated their interaction and stability. The CEP78 trimer is important for the

506   regulation of centriole and cilia length. Our study explains the etiology and

507   animal model of the syndrome of CRD and male infertility, provides basis for

24

508   molecular diagnosis, and serves as a potential target for gene therapy.

509 **Materials and Methods**

510 **Ethnical statement**

511   Our study, conformed to the Declaration of Helsinki, was prospectively

512 reviewed and approved by the ethics committee of Ningxia Eye Hospital and

513 Nanjing Medical University. Signed informed consents were obtained from all

514 individuals in the study.

515

516 **Mouse breeding**

517   All mice were raised in a specific-pathogen-free animal facility

518 accredited by Association for Assessment and Accreditation of Laboratory

519 Animal Care (AAALAC) in Model Animal Research Center, Nanjing

520 University, China. The facility provided ultraviolet sterilization, a 12-hour

521 light/dark cycle, ad libitum access to water, and standard mouse chow diet.

522 Mice experiments were performed in accordance with approval of the

523 Institutional Animal Care and Use Committee of Nanjing Medical University

524 and with the ARVO Statement for the Use of Animals in Ophthalmic and

525 Vision Research.

526

527 **Construction of *Cep78* deficient mice using CRISPR/Cas9**

528   CRISPR/Cas9 technology was applied to generate *Cep78* frameshift

529 mutations in mice using the non-homolog recombination method. Single-

530 guide RNAs (sgRNA) were designed against exons 2 to 11 of *Cep78*. Cas9

26

531   mRNA and sgRNAs were synthesized by *in vitro* transcription assay and

532   microinjected into the cytoplasm of single-cell C57BL/6J zygotes. The

533   injected embryos were then transferred into oviducts of pseudopregnant

534   female mice. Generated founder mice and their progenies were genotyped

535   by sequence analyses of the genomic DNA isolated by mice ear clipping to

536   screen for the frameshift mutation in *Cep78*. Genotyping was performed

537   using primer pairs for *Cep78*-null allele with an expected produce size of

538   ~400 bp and wild type *Cep78* allele with an expected produce size of 517 bp.

539   Primer sequences were listed in **Supplementary Table S5**. Identified

540   founder mice were crossed with wild type C57BL/6J mice to produce F1

541   progenies. Homozygote $Cep78^{-/-}$ mice were screened from F2 progenies

542   generated by inbreeding of F1 heterozygote progenies.

543

544   **Cell culture and transfection**

545   HEK293T and 3T3 cells were maintained in DMEM medium

546   supplemented with 10% fetal bovine serum (Invitrogen), penicillin (100U/mL)

547   and streptomycin (100g/mL) at 37°C, 5% CO_2. The open reading frame

548   sequences of mice *Cep78*, *Ift20* and *Ttc21a* were synthesized, amplified and

549   inserted into the pcDNA3.1 plasmid (GenScript, Nanjing, China) with HA/Flag

550   sequences in-frame fused to produce recombinant plasmids Cep78-HA,

551   Ift20-Flag, Ift20-HA and Ttc21a-Flag, respectively. Scramble siRNA, Cep78-

552   siRNA, Ift20-siRNA and Ttc21a-siRNA were purchased from GenePharma

553 (GenePharma, Shanghai, China) with their sequences listed in

554 **Supplementary Table S6**. Transfection assay was conducted using Exfect$^{®}$

555 transfection reagent (Vazyme, Nanjing, China).

556

557 **Immunoblotting**

558 Immunoblotting was conducted according to a previously defined

559 protocol[35, 36]. Mice neural retina and testes were isolated for

560 immunoblotting respectively. Collected tissues were ground in ice-cold

561 protein lysis buffer (Beyotime, Shanghai, China) containing protease

562 inhibitors cocktail (Roche, Basel, Switzerland) for protein extraction. The

563 lysates were separated on 10% sodium dodecyl sulfate-polyacrylamide gel,

564 and then transferred to a polyvinylidene fluoride membrane (Millipore,

565 Billerica, MA, USA). Membranes were then blocked with 5% skim milk at

566 37°C for one hour, incubated with primary antibodies at 4°C overnight

567 (**Supplementary Table S7**), washed with 1 × tris-buffered saline tween, and

568 probed with corresponding horse radish peroxidase-conjugated secondary

569 antibodies (dilution: 1:10000; ICL Inc., Newberg, Germany) at room

570 temperature for one hour. Blots were developed using the ECL-Western

571 blotting system (Bio-Rad, Hercules, CA, USA).

572

573 **ERG**

574 Mice were anesthetized intraperitoneally with a mixture of ketamine (100

28

575   mg/kg) and xylazine (10 mg/kg). Pupils were dilated with 1% cyclopentolate-

576   HCL and 2.5% phenylephrine. After dark adaption for 8 hours, ERG was

577   recorded under dim red light using an Espion system (Diagnosys LLC,

578   Lowell, MA, USA) in accordance with recommendations of the International

579   Society for Clinical Electrophysiology of Vision. ERG waves were

580   documented in response to flashes at 0.01, 3.0 and 10.0 cd×s/m^2.

581

582   **SD-OCT**

583   Mice anesthetization and pupil dilation were conducted as above

584   mentioned. Lateral images from nasal retina to temporal retina crossing

585   through the optic nerve were collected using a SD-OCT system (OptoProbe,

586   Burnaby, Canada). Thicknesses of retinal layers were measured by

587   Photoshop software (Adobe, San Jose, CA, USA) in a double-blind manner.

588

589   **Immunofluorescence staining**

590   Immunofluorescence staining was performed per a previously described

591   protocol[35, 36]. Mice eyecups and testicular tissues were enucleated after

592   sacrifice, rinsed with 1×phosphate buffer saline (PBS) with connective

593   tissues trimmed, and fixed in 4% paraformaldehyde (PFA) at 4°C overnight.

594   For eyecups, corneas and lens were subsequently removed without

595   disturbing the retina. Posterior eyecups and testicular tissues were then

596   dehydrated in 30% sucrose for 2 hours, embedded in optimal cutting

597   temperature compound, and frozen sectioned at 5 μm. For *in vitro* assay,

598   3T3 cells were collected at 48 hours post transfection and fixed in 4% PFA at

599   4°C overnight. Retinal, testicular and cellular sections were then blocked in

600   2% normal goat serum and permeabilized with 0.3% Triton X-100 at room

601   temperature for 1 hour. Those sections were further incubated with primary

602   antibodies (**Supplementary Table S7**) at 4°C overnight, and corresponding

603   fluorescence-conjugated secondary antibodies (dilution: 1:1000; Invitrogen,

604   Carlsbad, CA, USA) at room temperature for 1 hour. Nuclei were

605   counterstained with 4', 6-diamidino-2-phenylindole (DAPI; Sigma, St. Louis,

606   MO, USA). Retinal images were collected with a Leica TCS SP5 confocal

607   system (Leica), and testicular and cellular images were taken by an LSM 800

608   confocal microscope (Carl Zeiss, Jena, Germany).

609

610   **TEM and SEM assays**

611   Mice eyecups, mice semen cells collected from shredded unilateral

612   caudal epididymis, mice testicular tissues, and human ejaculated sperm

613   were subjected to TEM assay, respectively. Tissues were fixed in 2.5%

614   glutaradehyde at 4°C overnight immediately after enucleation. Eyecups were

615   dissected as described for TEM, and only the remaining posterior eyecups

616   were used for the following experiments. Samples were then post-fixed in 1%

617   osmic acid at 4°C for an hour, stained in aqueous 3% uranyl acetate for 2

618   hours, dehydrated with ascending concentrations of acetone, embedded in

619 epoxy resin, cut into ultra-thin slides, and stained in 0.3% lead citrate.

620 Ultrastructure of mice retina and human spermatozoa was visualized using a

621 JEM-1010 electron microscope (JEOL, Tokyo, Japan). Ultrastructure of mice

622 spermatids cells were observed with a Philips CM100 electron microscope

623 (Philips, Amsterdam, North-Holland). Ultrastructure of testicular tissues was

624 visualized using a FEI Tecnai G2 Spirit Bio TWIN electron microscope

625 (Thermo, Waltham, MA, USA).

626 For SEM assay, mice sperms collected from shredded unilateral caudal

627 epididymis and human ejaculated sperm were used. Human and mice

628 spermatozoa were immersed in 2.5% glutaraldehyde at 4°C overnight, fixed

629 in 1% osmic acid supplemented with 1.5% $K_3[Fe(CN)_3]$ at 4°C for an hour,

630 steeped in 1% thiocarbohydrazide for an hour, post-fixed in 1% osmic acid at

631 4°C for an hour, and soaked in 2% uranyl acetate solution at 4°C overnight.

632 The treated samples were then progressively dehydrated with an ethanol

633 and isoamyl acetate gradient on ice, and dried with a CO2 critical-point dryer

634 (Eiko HCP-2, Hitachi Ltd., Toyko, Japan). The specimens were subsequently

635 mounted on aluminum stubs, sputtercoated by an ionic sprayer meter (Eiko

636 E-1020, Hitachi Ltd.), and visualized using a FEI Nova NanoSEM 450

637 scanning electron microscope (Thermo).

638

639 **CASA and sperm morphological study**

640 Mice sperms, collected from shredded unilateral caudal epididymis,

31

641 were maintained in 500 μL modified human tubal fluid (Irvine Scientific,

642 Santa Ana, CA, USA) supplemented with 10% fetal bovine serum (Gibco,

643 Grand Island, NY, USA) at 37 °C for 7 min. Sperm concentration, motility,

644 and progressive motility of semen samples were then assessed by CASA

645 (IVOS II, Hamilton Thorne Inc., Beverly, MA, USA).

646 Human ejaculated semen sample was collected by masturbation after 7

647 days of sexual abstinence. Semen volume was measured with test tube.

648 After liquefaction at 37 °C for 30 min, semen sample was further subjected to

649 CASA (BEION S3-3, BEION, Beijing, China) for measurement of sperm

650 concentration, motility and progressive motility per the 5th edition of World

651 Health Organization (WHO) guidelines.

652 Human and mice semen samples were stained on slides using the H&E

653 staining method for sperm morphological analyses. At least 150

654 spermatozoa were analyzed for each group. Percentages of spermatozoa

655 with normal morphology, abnormal head, abnormal neck and abnormal

656 flagella were calculated per the WHO guidelines. Abnormalities of sperm

657 flagella were further classified into 7 categories, including short flagella,

658 absent flagella, coiled flagella, multi flagella, cytoplasm remain, irregular

659 caliber, and angulation. Noteworthy, one spermatozoon was sorted into only

660 one group based on its major flagellar abnormality.

661

662 **Histological H&E staining**

32

663   For histological H&E staining, mice epididymal tissues and sperms

664   collected from shredded unilateral caudal epididymis were rinsed with

665   1×PBS, fixed in 4% PFA at 4°C overnight, dehydrated with ascending

666   concentrations of ethanol, embedded in paraffin, and sectioned into 5 μm

667   slides. Slides were then deparaffinized in xylene, rehydrated with decreasing

668   concentrations of ethanol, and stained with hematoxylin and eosin for

669   histological observation. Images were taken with a Zeiss Axio Skop plus2

670   microscope (Carl Zeiss).

671

672   **PAS staining**

673   PAS staining was used for spermatogenic staging and evaluation of the

674   development of seminiferous tubules. Fresh mice testicular tissues were

675   fixed with modified Davidson's fluid (mDF) fixation fluid at room temperature

676   for 48 hours, embedded with paraffin, and sliced into sections. Slides were

677   then dewaxed with xylene at 37°C for 30 min, rehydrated by descending

678   concentrations of ethanol, dyed with periodic acid, Schiff (Solarbio, Beijing,

679   China) and hematoxylin in sequence, dehydrated with ascending

680   concentrations of ethanol, and sealed with neutral balsam for observation.

681   Images were taken with a Zeiss Axio Skop plus2 microscope (Carl Zeiss).

682

683   **Sample preparation, IP, and MS analyses**

684   Testicular tissues of $Cep78^{+/-}$ and $Cep78^{-/-}$ mice were lysed with Pierce^{TM}

685   IP lysis buffer (Thermo) supplemented with 1% protease inhibitor cocktail

686   100X (Selleck Chemicals, Houston, TX, USA), respectively. Lysates were

687   revolved for 1 hour at 4°C and centrifuged at 40000g for 1 hour.

688   Supernatants were precleared with 20 µL of protein A/G magnetic beads

689   (Millipore) at 4°C for 1 hour. IP was performed using the Pierce™ co-IP kit

690   (Thermo). Eluted proteins were then subjected to SDS-PAGE, silver stain,

691   immunoblotting and MS. For MS, silver stained gel lanes were carefully cut

692   into small pieces and were then processed for MS analysis. Briefly, after

693   trypsin digestion overnight, peptides were desalted using stage tips, re-

694   suspended in 0.1% formic acid (v/v) and subjected to LC-MS[37-40]. Data of

695   IP-MS was submitted to Dryad, Dataset,

696   https://doi.org/10.5061/dryad.6djh9w12z.

697   .

698   For quantitative mass spectrometry (MS) on elongating spermatids

699   lysates of $Cep78^{+/-}$ and $Cep78^{-/-}$ mice, lysed samples were digested

700   overnight at 37 ◦C with trypsin and subjected to the TMT labeling. For MS

701   analyses, each fraction was analyzed using an Orbitrap Fusion Lumos mass

702   spectrometer (Thermo Finnigan, San Jose, CA) coupled with Easy-nLC 1200

703   (Thermo Finnigan, San Jose, CA), and was separated by a High PH reverse

704   phase saperation microcapillary column (ACQUITY BEH C18 Column, 1.7

705   µm, 300µm X 150 mm) at a flow rate of 4µL/min in a 128-min linear gradient

706   (3% buffer B for 14 min, 8% buffer B for 1 min, 29% buffer B for 71 min, 41%

707 buffer B for 12 min, 100% buffer B for 9 min, 3% buffer B for 21 min) (solvent

708 A: 20mM Ammonium formate, PH=10; solvent B: 100% ACN, 0.1% FA).

709 Sample were collected at a rate of one tube per minute, a total of 30

710 components. Easy1200 and fusion Lumos were used for series identification.

711 Data of quantitative mass spectrometry (MS) on elongating spermatids

712 lysates was submitted to Dryad, Dataset, https://doi.org/10.5061/dryad.stqjq2c4p

713

714

715 **co-IP assay**

716 HEK293T cells were collected at 48 hours post transfection, and lysed

717 with Pierce^{TM} IP lysis buffer (Thermo) supplemented with 1% protease

718 inhibitor cocktail 100X (Selleck Chemicals). Lysates was revolved for 30

719 minutes at 4°C and centrifuged at 16000g for 30 minutes. Supernatants were

720 incubated with 30 µL of Pierce^{TM} anti-HA magnetic beads (Thermo) or anti-

721 DYKDDDDK IP resin (GenScript) at 4°C overnight. IP was performed using

722 the Pierce^{TM} co-IP kit (Thermo), and eluted proteins were further subjected to

723 immunoblotting.

724

725 **RNA extraction and Q-PCR**

726 3T3 cells were harvested at 48 hours post transfection for RNA

727 extraction. Total RNA was isolated from lysates of transfected 3T3 cells using

728 TRIzol reagent (Invitrogen). RNA concentration and quality were determined

729   with Nano-Drop ND-1000 spectrophotometer (Nano-Drop Technologies,

730   Wilmington, DE, USA). cDNA was generated with a PrimeScript RT Kit

731   (Takara, Otsu, Shiga, Japan). Q-PCR was conducted to detect RNA amounts

732   using FastStart Universal SYBR Green Master (ROX; Roche, Basel,

733   Switzerland) with StepOne Plus Real-Time PCR System (Applied

734   Biosystems, Darmstadt, Germany). Primer sequences were listed in

735   **Supplementary Table S5**.

736

737   **Statistical analysis**

738   GraphPad Prism (version 8.0; GraphPad Software, San Diego, CA,

739   USA) was applied for statistical analyses. Student's t test was utilized for

740   comparisons between two different groups. One-way analysis of variance

741   (ANOVA) followed by Dunnet´s multiple comparison test was applied for

742   comparisons among three or more groups. We presented data as mean ±

743   standard error of the mean, and considered $p < 0.05$ as statistically

744   significant. All experiments were conducted in both biological and technical

745   triplicates with data averaged.

746

Acknowledgements

757 **Author Contributions**

758   X.C., X.G. and C.Z. conceived and designed the study. T.Z. and Y.Z.

759 conducted experiments. T.Z and X.C. interpreted the data and drafted the

760 manuscript. X.G. and C.Z. revised the manuscript. X.S., X.Z., Y.C., Y.S., and

761 Y.Q. coordinated and analyzed the data. All the authors contributed to, read,

762 and approved the final manuscript.

763

764 **Declaration of Interests Statements**

765   The authors have declared that no competing interest exists.

766

References

1. Gill, J.S., et al., *Progressive cone and cone-rod dystrophies: clinical features, molecular genetics and prospects for therapy.* Br J Ophthalmol, 2019.

2. Kubota, D., et al., *CEP250 mutations associated with mild cone-rod dystrophy and sensorineural hearing loss in a Japanese family.* Ophthalmic Genet, 2018. **39**(4): p. 500-507.

3. Charbel Issa, P., et al., *Olfactory Dysfunction in Patients With CNGB1-Associated Retinitis Pigmentosa.* JAMA Ophthalmol, 2018. **136**(7): p. 761-769.

4. Yildiz Bolukbasi, E., et al., *Homozygous mutation in CEP19, a gene mutated in morbid obesity, in Bardet-Biedl syndrome with predominant postaxial polydactyly.* J Med Genet, 2018. **55**(3): p. 189-197.

5. Brunk, K., et al., *Cep78 is a new centriolar protein involved in Plk4-induced centriole overduplication.* J Cell Sci, 2016. **129**(14): p. 2713-8.

6. Hossain, D., et al., *Cep78 controls centrosome homeostasis by inhibiting EDD-DYRK2-DDB1(Vpr)(BP).* EMBO Rep, 2017. **18**(4): p. 632-644.

7. Azimzadeh, J., et al., *Centrosome loss in the evolution of planarians.* Science, 2012. **335**(6067): p. 461-3.

8. Fu, Q., et al., *CEP78 is mutated in a distinct type of Usher syndrome.* J Med Genet, 2017. **54**(3): p. 190-195.

9. Nikopoulos, K., et al., *Mutations in CEP78 Cause Cone-Rod Dystrophy and Hearing Loss Associated with Primary-Cilia Defects.* Am J Hum Genet, 2016. **99**(3): p. 770-776.

10. Namburi, P., et al., *Bi-allelic Truncating Mutations in CEP78, Encoding Centrosomal Protein 78, Cause Cone-Rod Degeneration with Sensorineural Hearing Loss.* Am J Hum Genet, 2016. **99**(3): p. 777-784.

11. Sanchis-Juan, A., et al., *Complex structural variants in Mendelian disorders: identification and breakpoint resolution using short- and long-read genome sequencing.* Genome Med, 2018. **10**(1): p. 95.

12. Ascari, G., et al., *Functional characterization of the first missense variant in CEP78, a founder allele associated with cone-rod dystrophy, hearing loss, and reduced male fertility.* Hum Mutat, 2020.

13. Zhang, M., et al., *Low expression of centrosomal protein 78 (CEP78) is associated with poor prognosis of colorectal cancer patients.* Chin J Cancer, 2016. **35**(1): p. 62.

14. Nesslinger, N.J., et al., *Standard treatments induce antigen-specific immune responses in prostate cancer.* Clin Cancer Res, 2007. **13**(5): p. 1493-502.

15. Goncalves, A.B., et al., *CEP78 functions downstream of CEP350 to control biogenesis of primary cilia by negatively regulating CP110 levels.* Elife, 2021. **10**.

16. Bedoni, N., et al., *Mutations in the polyglutamylase gene TTLL5, expressed in photoreceptor cells and spermatozoa, are associated with cone-rod degeneration and reduced male fertility.* Hum Mol Genet, 2016. **25**(20): p. 4546-4555.

17. Liu, W., et al., *Bi-allelic Mutations in TTC21A Induce Asthenoteratospermia in Humans and Mice.* Am J Hum Genet, 2019. **104**(4): p. 738-748.

18. Keady, B.T., Y.Z. Le, and G.J. Pazour, *IFT20 is required for opsin trafficking and photoreceptor outer segment development.* Mol Biol Cell, 2011. **22**(7): p. 921-30.

19. Zhang, Z., et al., *Intraflagellar transport protein IFT20 is essential for male fertility and*

810   *spermiogenesis in mice.* Mol Biol Cell, 2016.

811   20.   Zhu, X., et al., *Mouse cone arrestin expression pattern: light induced translocation in cone*
812   *photoreceptors.* Mol Vis, 2002. **8**: p. 462-71.

813   21.   Avidor-Reiss, T. and E.L. Fishman, *It takes two (centrioles) to tango.* Reproduction, 2019.
814   **157**(2): p. R33-R51.

815   22.   Kierszenbaum, A.L. and L.L. Tres, *The acrosome-acroplaxome-manchette complex and the*
816   *shaping of the spermatid head.* Arch Histol Cytol, 2004. **67**(4): p. 271-84.

817   23.   Fu, Q., et al., *CEP78 is mutated in a distinct type of Usher syndrome.* J Med Genet, 2017.
818   **54**(3): p. 190-195.

819   24.   Chaki, M., et al., *Exome capture reveals ZNF423 and CEP164 mutations, linking renal*
820   *ciliopathies to DNA damage response signaling.* Cell, 2012. **150**(3): p. 533-48.

821   25.   Valente, E.M., et al., *Mutations in CEP290, which encodes a centrosomal protein, cause*
822   *pleiotropic forms of Joubert syndrome.* Nat Genet, 2006. **38**(6): p. 623-5.

823   26.   Baala, L., et al., *Pleiotropic effects of CEP290 (NPHP6) mutations extend to Meckel*
824   *syndrome.* Am J Hum Genet, 2007. **81**(1): p. 170-9.

825   27.   den Hollander, A.I., et al., *Mutations in the CEP290 (NPHP6) gene are a frequent cause of*
826   *Leber congenital amaurosis.* Am J Hum Genet, 2006. **79**(3): p. 556-61.

827   28.   Karlstetter, M., et al., *Disruption of the retinitis pigmentosa 28 gene Fam161a in mice affects*
828   *photoreceptor ciliary structure and leads to progressive retinal degeneration.* Hum Mol
829   Genet, 2014. **23**(19): p. 5197-210.

830   29.   Lehti, M.S. and A. Sironen, *Formation and function of the manchette and flagellum during*
831   *spermatogenesis.* Reproduction, 2016. **151**(4): p. R43-54.

832   30.   Kierszenbaum, A.L., et al., *Ran, a GTP-binding protein involved in nucleocytoplasmic*
833   *transport and microtubule nucleation, relocates from the manchette to the centrosome*
834   *region during rat spermiogenesis.* Mol Reprod Dev, 2002. **63**(1): p. 131-40.

835   31.   Akhmanova, A., et al., *The microtubule plus-end-tracking protein CLIP-170 associates with*
836   *the spermatid manchette and is essential for spermatogenesis.* Genes Dev, 2005. **19**(20): p.
837   2501-15.

838   32.   Kierszenbaum, A.L., E. Rivkin, and L.L. Tres, *Cytoskeletal track selection during cargo*
839   *transport in spermatids is relevant to male fertility.* Spermatogenesis, 2011. **1**(3): p. 221-
840   230.

841   33.   Zhang, Z., et al., *Intraflagellar transport protein IFT20 is essential for male fertility and*
842   *spermiogenesis in mice.* Mol Biol Cell, 2016. **27**(23): p. 3705-16.

843   34.   Kazarian, E., et al., *SPAG17 Is Required for Male Germ Cell Differentiation and Fertility.* Int J
844   Mol Sci, 2018. **19**(4).

845   35.   Jiang, C., et al., *MicroRNA-184 promotes differentiation of the retinal pigment epithelium by*
846   *targeting the AKT2/mTOR signaling pathway.* Oncotarget, 2016. **7**(32): p. 52340-52353.

847   36.   Liu, Y., et al., *SPP2 Mutations Cause Autosomal Dominant Retinitis Pigmentosa.* Sci Rep,
848   2015. **5**: p. 14867.

849   37.   Guo, X., et al., *Proteomic analysis of male 4C germ cell proteins involved in mouse meiosis.*
850   Proteomics, 2011. **11**(2): p. 298-308.

851   38.   Guo, X., et al., *Proteomic analysis of proteins involved in spermiogenesis in mouse.* J
852   Proteome Res, 2010. **9**(3): p. 1246-56.

853   39.   Hu, Z., et al., *A genome-wide association study identifies two risk loci for congenital heart*

854   *malformations in Han Chinese populations.* Nat Genet, 2013. **45**(7): p. 818-21.
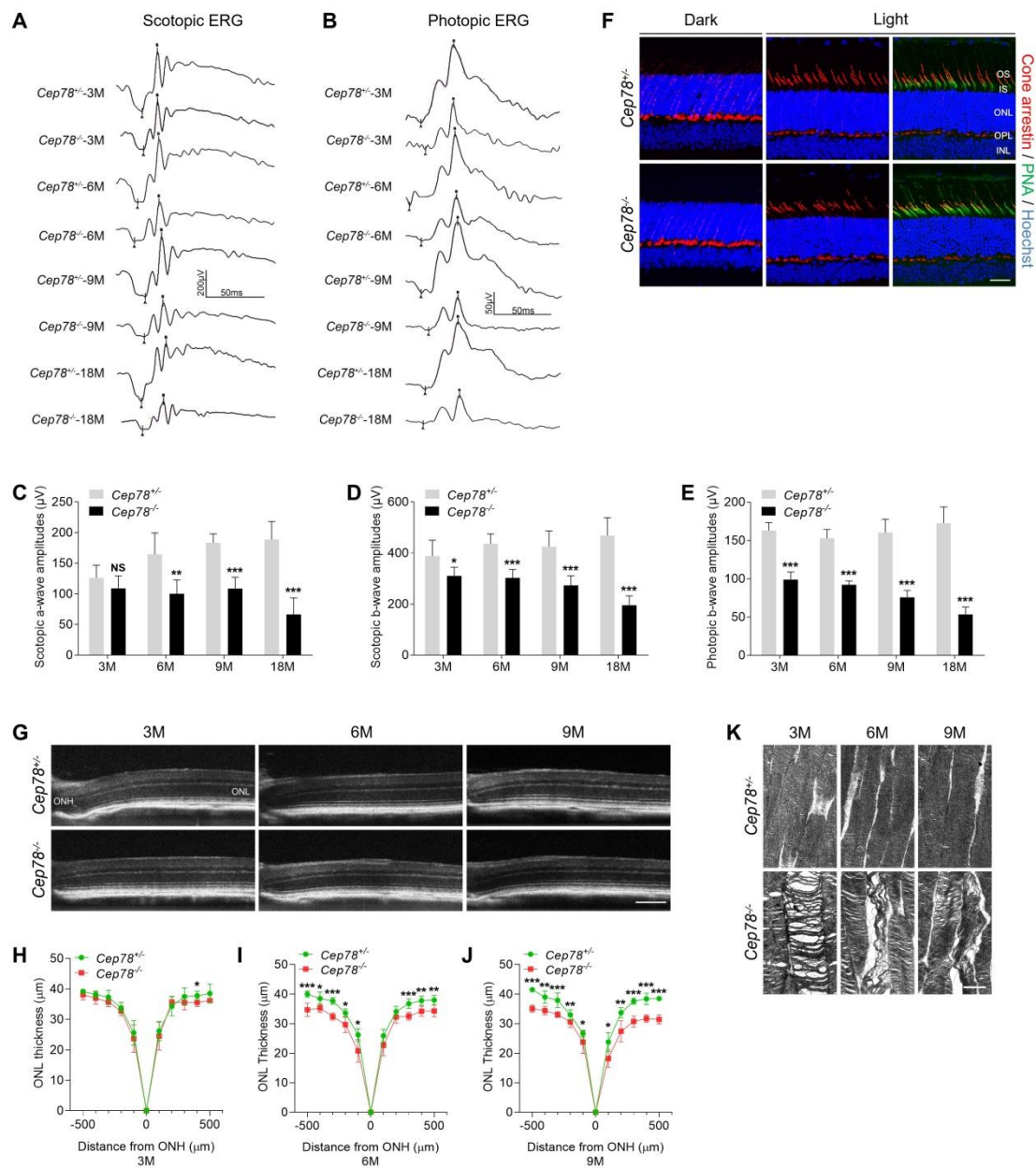
855   40.   Fan, Y., et al., *Phosphoproteomic Analysis of Neonatal Regenerative Myocardium Revealed*

856   *Important Roles of Checkpoint Kinase 1 via Activating Mammalian Target of Rapamycin*

857   *C1/Ribosomal Protein S6 Kinase b-1 Pathway.* Circulation, 2020. **141**(19): p. 1554-1569.

858

Figures

Figure 1. *Cep78* deletion leads to photoreceptor impairments in mice retina. (A-E) Scotopic and photopic ERG of *Cep78⁻/⁻* mice at the indicated ages. Representative images along with the quantification results were shown (n=6 for each sample, two-tailed Student's t test). NS, not significant. *, $p < 0.05$, **, $p < 0.01$, ***, $p < 0.001$. (F) Immunofluorescence staining showing expression patterns of cone arrestin (CAR) and peanut agglutinin (PNA) lectin in dark- and light-adapted retinas of *Cep78⁺/⁻* and *Cep78⁻/⁻* mice at 3-month. Scale bar, 25 μm. (G-J) SD-OCT revealed thickness of outer nucleic layer (ONL) in retinas of *Cep78⁺/⁻* and *Cep78⁻/⁻* mice of indicated ages. Scale bar, 150 μm. Representative images along with the

43

871   quantification results were shown (n=6 for each sample, two-tailed Student's

872   t test). *, $p < 0.05$, **, $p < 0.01$, ***, $p < 0.001$. (K) TEM revealed ultra-

873   structures of photoreceptors in *Cep78$^{+/-}$* and *Cep78$^{-/-}$* mice at the indicated

874   ages. Scale bar, 1 μm.

875
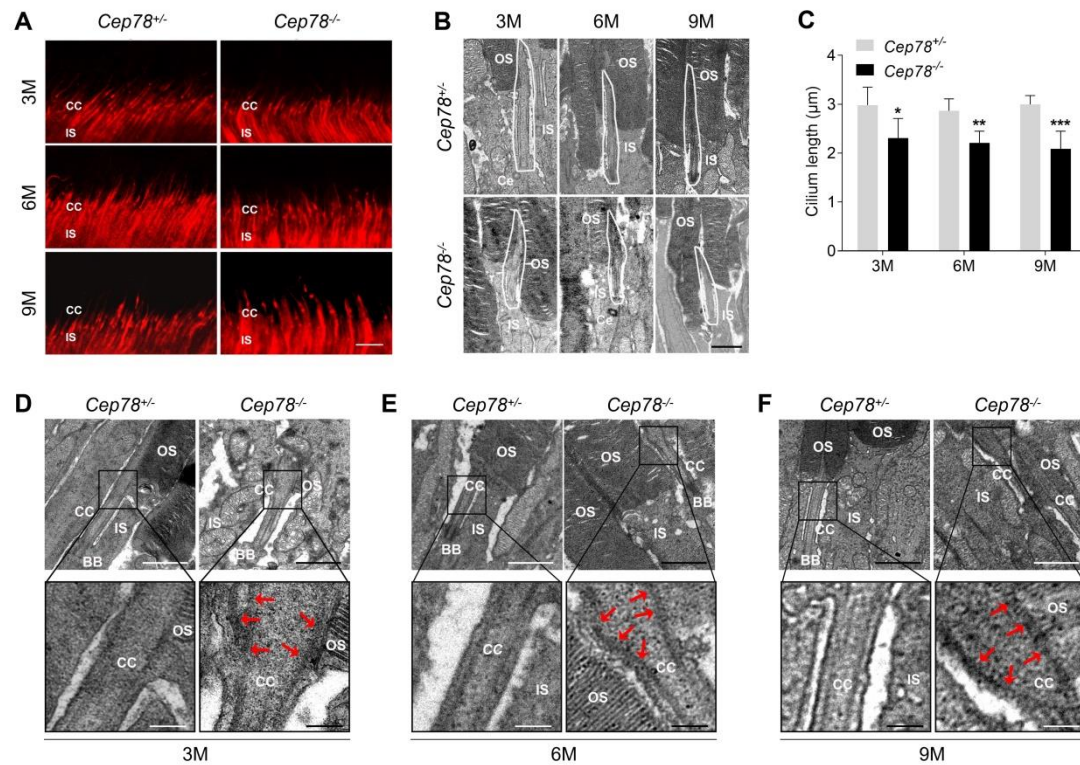
Figure 2. Cep78$^{-/-}$ mice exhibit disturbed ciliary structure in photoreceptors. (A) Retinal cryosections from Cep78$^{+/-}$ and Cep78$^{-/-}$ mice at indicated ages stained with Ac-α-tubulin (red) to visualize ciliary axonemes and basal bodies. Scale bar, 5 µm. CC, connecting cilium; IS, inner segment. (B-C) TEM was applied to observe longitudinal sections of the ciliary region of photoreceptors in Cep78$^{+/-}$ and Cep78$^{-/-}$ mice at indicated ages. Scale bar, 1 µm. OS, outer segment; IS, inner segment; Ce, Centriole. n=6 for each sample, *, $p < 0.05$, **, $p < 0.01$, ***, $p < 0.001$. (D-F) TEM was used to observe the ultrastructure of connecting cilium in photoreceptors of Cep78$^{+/-}$ and Cep78$^{-/-}$ mice at indicated ages. Scale bar, upper 1 µm, below 200 nm. OS, outer segment; CC, connecting cilium; IS, inner segment; BB, basal body.

890
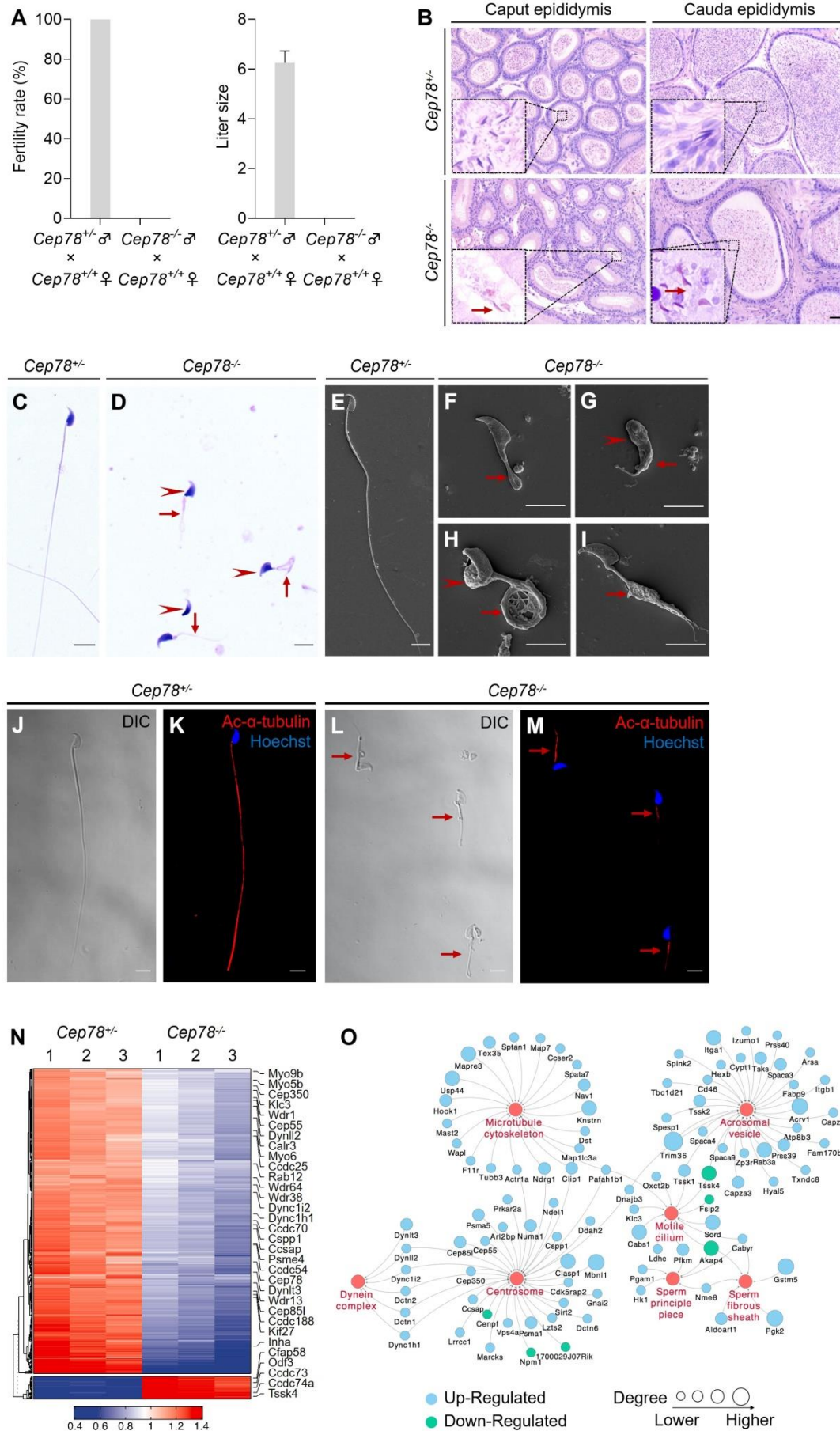
891 **Figure 3. *Cep78^{-/-}* mice present male infertility and morphological**

892 **abnormalities of sperm.** (A) Fertility rates (left) and litter sizes (right) of

893 *Cep78^{+/-}* and *Cep78^{-/-}* male mice crossed with *Cep78^{+/+}* female mice, n=4 for

894 *Cep78^{+/-}* male mice crossed with *Cep78^{+/+}* female mice, n=5 for *Cep78^{+/-}*

895 male mice crossed with *Cep78^{+/+}* female mice. (B) H&E staining was utilized

896 to observe the structures of caput and cauda epididymis in *Cep78^{+/-}* and

897 *Cep78^{+/-}* mice. Scale bar, 100 μm. (C-D) Spermatozoa from *Cep78^{+/-}* (C) and

898 *Cep78^{-/-}* (D) mice were observed with H&E staining. Abnormal heads and

899 short, missing or coiled flagella were indicated by arrow heads and arrows

900 respectively. Scale bar, 5 μm. (E-I) Spermatozoa of *Cep78^{+/-}* (E) and *Cep78^{-/-}*

901 (F-I) mice were observed by SEM. Abnormal heads were represented by

902 arrow heads. Absent, short, coiled or multi flagella were indicated by arrows.

903 (J-M) Spermatozoa of *Cep78^{+/-}* and *Cep78^{-/-}* mice were pictured using

904 differential interference contrast (J, L), and were stained with Ac-α-tubulin

905 (red) and Hoechst (blue) to visualize axonemes and heads, respectively (K,

906 M). (N) Heatmap showing differentially expressed proteins between *Cep78^{+/-}*

907 and *Cep78^{−/−}* mice elongating spermatids. (O) Network analysis of GO

908 cellular components terms enriched in differential expressed proteins

909 between *Cep78^{+/-}* and *Cep78^{−/−}* mice elongating spermatids. Scale bar, 5μm.

910

47
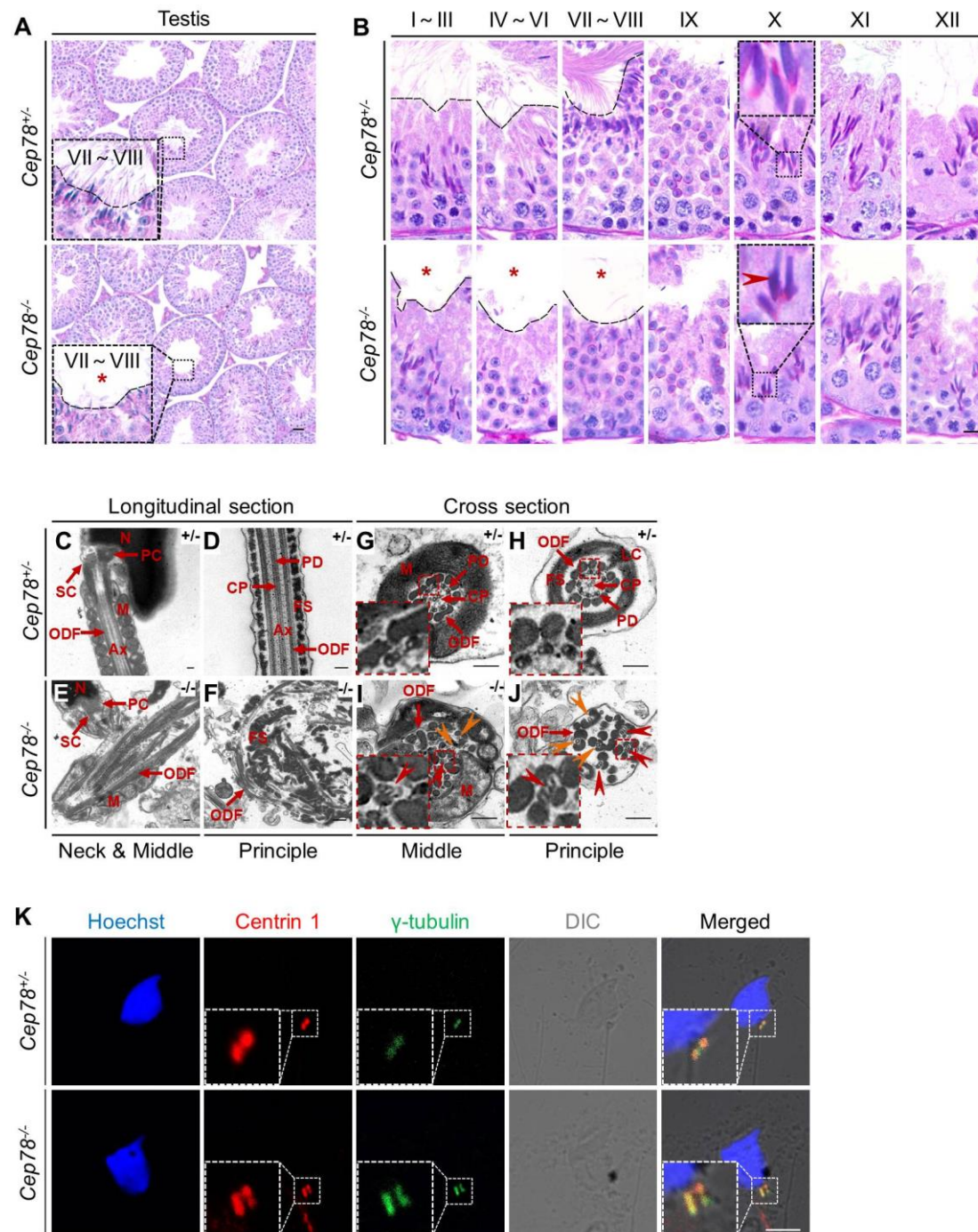
Figure 4. Defective microtubule arrangements and elongated centrioles in sperm flagella of Cep78$^{-/-}$ mice. (A) Paraffin sections of testicular tissues from Cep78$^{+/-}$ and Cep78$^{-/-}$ male mice were stained with PAS. Defects of sperm tails were indicated by asterisk. Scale bar, 50μm. (B) Twelve stages of spermatogenesis in Cep78$^{+/-}$ and Cep78$^{-/-}$ male mice were presented by PAS-stained paraffin sections of seminiferous tubules. Lack of sperm tails and abnormal nuclei shape of elongated spermatids were indicated by asterisk and arrow head, respectively. Schematic diagrams were attached. Scale bar, 10μm. (C-J) TEM was applied to visualize ultra-structures of

921   *Cep78*$^{+/-}$ and *Cep78*$^{-/-}$ spermatozoa in longitudinal sections of neck & middle

922   pieces (C and E) and principal pieces (D and F), and in cross sections of

923   middle pieces (G and I) and principal pieces (H and J). Triplet and singlet

924   microtubules were indicated by red and orange arrow heads (I-J),

925   respectively. Scale bar, 200 nm. (K) *Cep78*$^{+/-}$ and *Cep78*$^{-/-}$ mice spermatozoa

926   were stained with centrin 1 and γ-tubulin to reveal the structure of

927   centrosome. Scale bar, 5 μm.

928

929

Figure 5. *Cep78⁻ᐟ⁻* testes present abnormalities in spermatid head formation during spermiogenesis. (A) Sixteen steps of spermiogenesis in *Cep78⁺ᐟ⁻* and *Cep78⁻ᐟ⁻* male mice were presented by PAS-stained paraffin sections of seminiferous tubules. Lack of sperm tails and abnormal nuclei shape of elongated spermatids were indicated by asterisk and arrow head, respectively. Schematic diagrams were attached. Scale bar, 10μm. (B) Elongated spermatids from stage 9-14 from *Cep78⁺ᐟ⁻* and *Cep78⁻ᐟ⁻* mice were stained with PNA (red) and α-tubulin (green) to see elongation of manchette structures. Nuclei were counterstained with Hoechst (blue). Manchette structures were recognized by double-head arrows. Scale bar, 5μm. Schematic diagrams were attached. (C-M) TEM was used to visualize ultra-

50

941 structures of *Cep78*$^{+/-}$ and *Cep78*$^{-/-}$ spermiogenic spermatids from step 10-
942 14. Scale bar, 500 nm. N, nucleus; M, mitochondria; Ax, axoneme; SC,
943 segmented column of the connecting piece; PC, proximal centriole; ODF,
944 outer dense fiber; PD, peripheral microtubule doublets; CP, central pair of
945 microtubules; FS, fibrous sheath; LC, longitudinal column; Ac, acrosome; Pr,
946 perinuclear ring; Mt, manchette. Abnormal structures of manchette were
947 indicated by celeste arrow heads (D, E, H, I, K). Green arrow heads pointed
948 at abnormal bend of spermatid heads (E, F). Yellow arrow heads
949 represented abnormal acrosomes (I, L, M). Asterisk indicated expanded
950 perinuclear space (M). (N) Paraffin sections of testicular seminiferous tubules
951 from stage IX of spermatogenesis to stage I in *Cep78*$^{+/-}$ and *Cep78*$^{-/-}$ mice
952 were stained with transition protein 1 (red) and Hoechst (blue) to observe
953 nuclear condensation. Scale bar, 5μm. (O-P) Immunofluorescence staining
954 of γH2ax (red) and Sycp3 (green) in chromosome spreads of spermatocytes
955 from the testes of *Cep78*$^{+/-}$ and *Cep78*$^{-/-}$ mice. Scale bar, 5μm.
956 Representative image along with the quantification results was shown
957 (n=219 for Cep78$^{+/-}$ spermatocytes, n=208 for Cep78$^{-/-}$ spermatocytes, two-
958 tailed Student's t test, NS: not significant).
959
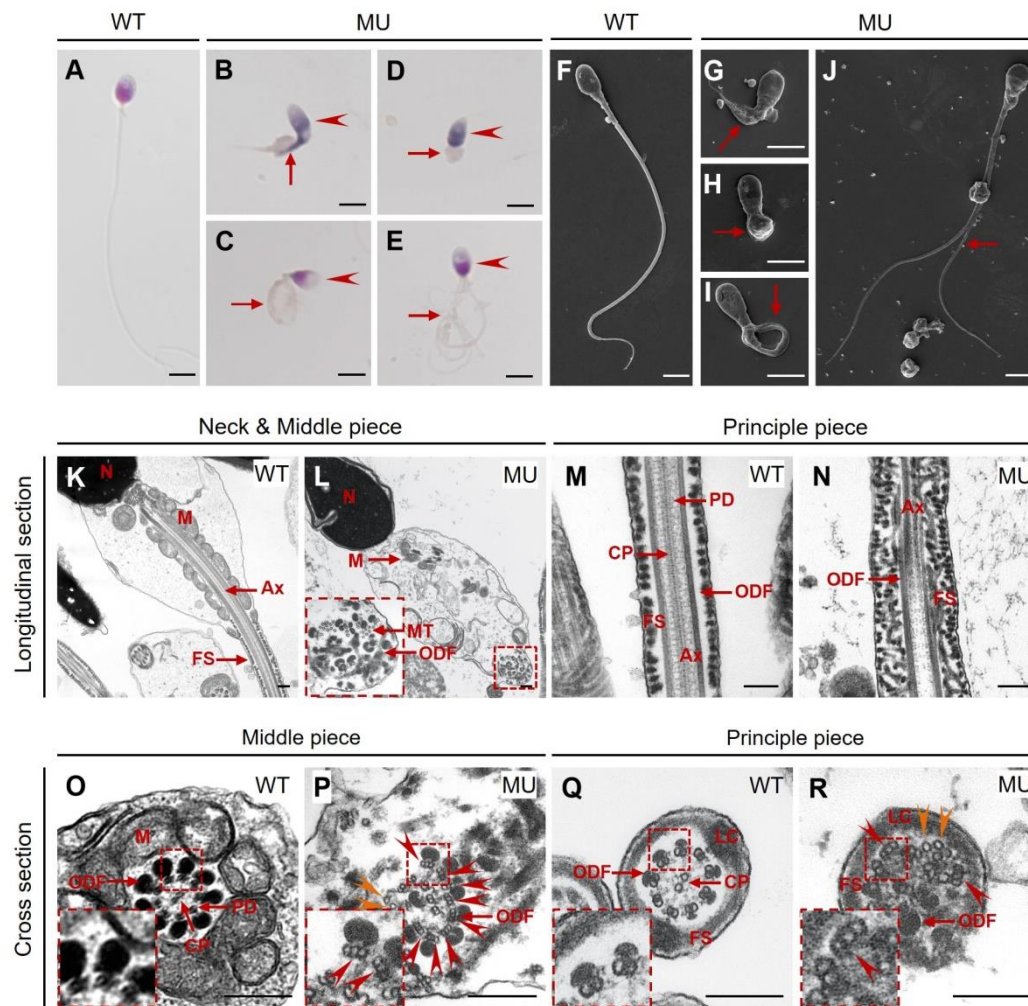
Figure 6. *CEP78* mutation causes MMAF phenotypes in human. (A-E) HE staining was utilized to see structures of spermatozoa from a healthy control (A) and a patient carrying homozygous *CEP78* c.1629-2A>G mutation (B-E). Scale bar, 5μm. Arrow heads represented abnormal sperm heads. Short, coiled, absent or multi flagella were indicated by arrows. (F-J) Ultra-structures of spermatozoa from the healthy control (F) and the patient with *CEP78* mutation (G-J) were observed using SEM. Short, coiled, absent or multi flagella, and cytoplasm remain were indicated by arrows. Scale bar, 5μm. (K-R) TEM was applied to visualize ultra-structures of spermatozoa from the healthy control and the patient in longitudinal sections of neck & middle pieces (K-L) and principal pieces (M-N), and in cross sections of middle pieces (O-P) and principal pieces (Q-R). Triplet and singlet microtubules were indicated by red and orange arrow heads (P, R), respectively. Scale bar, 200 nm (K-R). N, nucleus; M, mitochondria; MT, microtubules; Ax, axoneme; FS, fibrous sheath; ODF, outer dense fiber; PD, peripheral microtubule doublets; CP, central pair of microtubules; LC, longitudinal column.

978

979
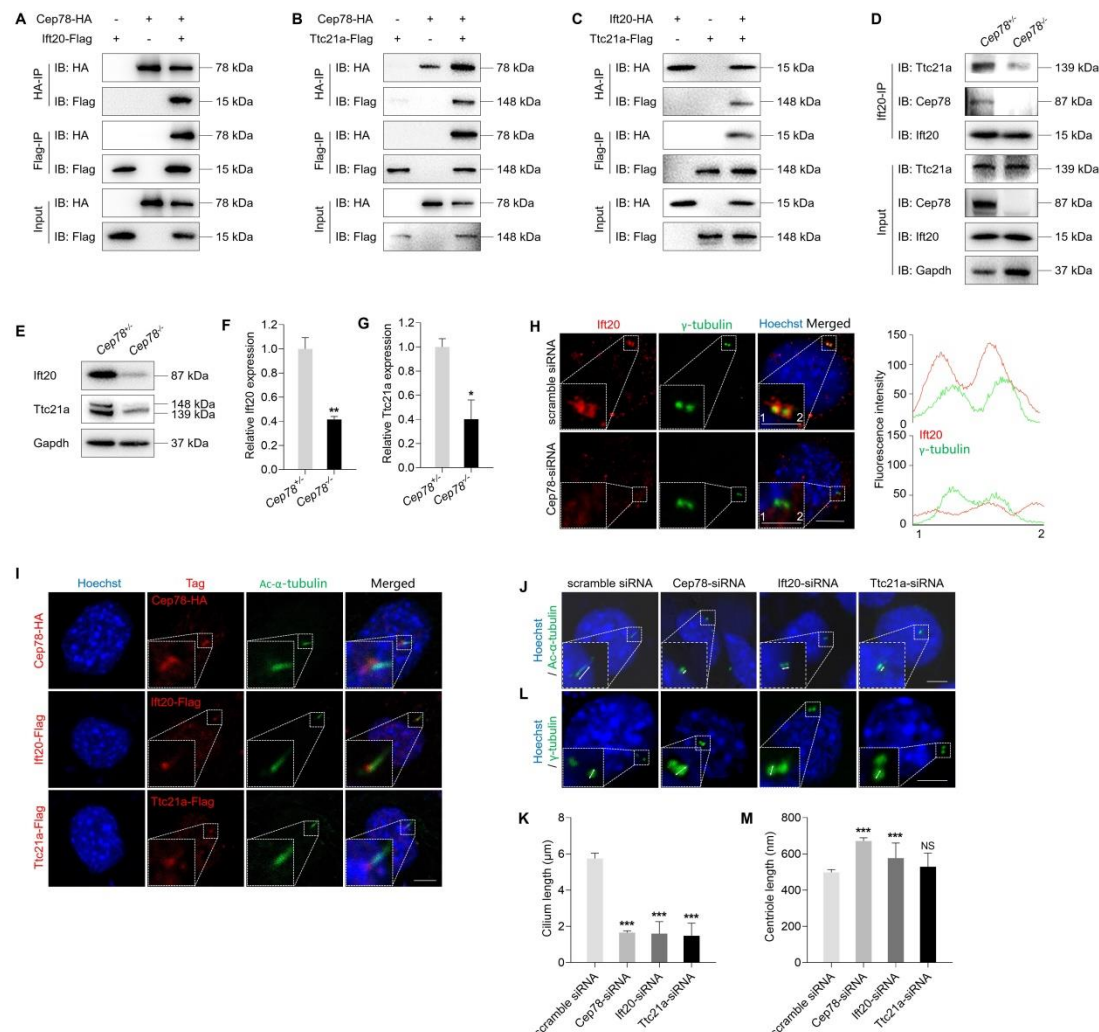
Figure 7. CEP78 forms a trimer with IFT20 and TTC21A to regulate axonemal and centrosomal elongations. (A-C) HEK293T cells were co-transfected with plasmids expressing Cep78-HA and Ift20-Flag (A), Cep78-HA and Ttc21a-Flag (B), or Ift20-HA and Ttc21a-Flag (C). Cellular lysates were immunoprecipitated with an anti-HA or anti-Flag antibody in 1% SDS and then immunoblotted (IB) with anti-HA or anti-Flag antibodies. (D) Lysates of testicular tissues from $Cep78^{+/-}$ and $Cep78^{-/-}$ male mice were immunoprecipitated with anti-Ift20 antibody in 1% SDS and then immunoblotted with anti-Ttc21a, anti-Cep78 or anti-Ift20 antibodies. (E-G) Immunoblotting showed Ift20 and Ttc21a expressions in lysates of testes from $Cep78^{+/-}$ and $Cep78^{-/-}$ mice (E). Representative images along with the quantification results were shown (F and G; 3 biological replications for $Cep78^{+/-}$ and $Cep78^{-/-}$ testes, two-tailed Student's t test). (H) 3T3 cells transfected with scramble siRNA or Cep78-siRNA were stained with Ift20 and γ-tubulin to reveal the intensities and locations of Ift20 and centrioles. Scale bar, 5 μm. A representative image of along with the quantification result was shown. (I) HA-tag, Flag-tag and cilia in 3T3 cells overexpressing Cep78-HA, Ift20-Flag or Ttc21a-Flag were visualized using antibodies against HA, Flag

54

998 and Ac-α-tubulin, respectively. Nuclei were counterstained with Hoechst
999 (blue). (J-M) Cilia (J) and centrioles (L) in 3T3 cells transfected with scramble
1000 siRNA, Cep78-siRNA, Ift20-siRNA or Ttc21a-siRNA were stained with Ac-α-
1001 tubulin and γ-tubulin respectively. Nuclei were counterstained with Hoechst
1002 (blue). Cilium and centriole structures were recognized by double-head
1003 arrows. Scale bar, 5μm. Representative images along with the quantification
1004 results were shown (K and M; Comparisons in cilia and centriole size
1005 between the scramble siRNA, Cep78 siRNA, Ift20 siRNA and Ttc21a siRNA
1006 were addressed by accumulated data from 3 independent experiments, for
1007 cilia length: n=35 for WT, n=34 for Cep78 siRNA,n=38 for Ift20 siRNA,n=40
1008 for Ttc21a siRNA;for centriole length: n=21 for WT, n=25 for Cep78
1009 siRNA,n=44 for Ift20 siRNA,n=55 for Ttc21a siRNA; one-way ANOVA, with
1010 Dunnet´s multiple comparison test amongst all groups). *, $p < 0.05$; **, $p <$
1011 0.01; ***, $p < 0.001$; NS, not significant.
1012
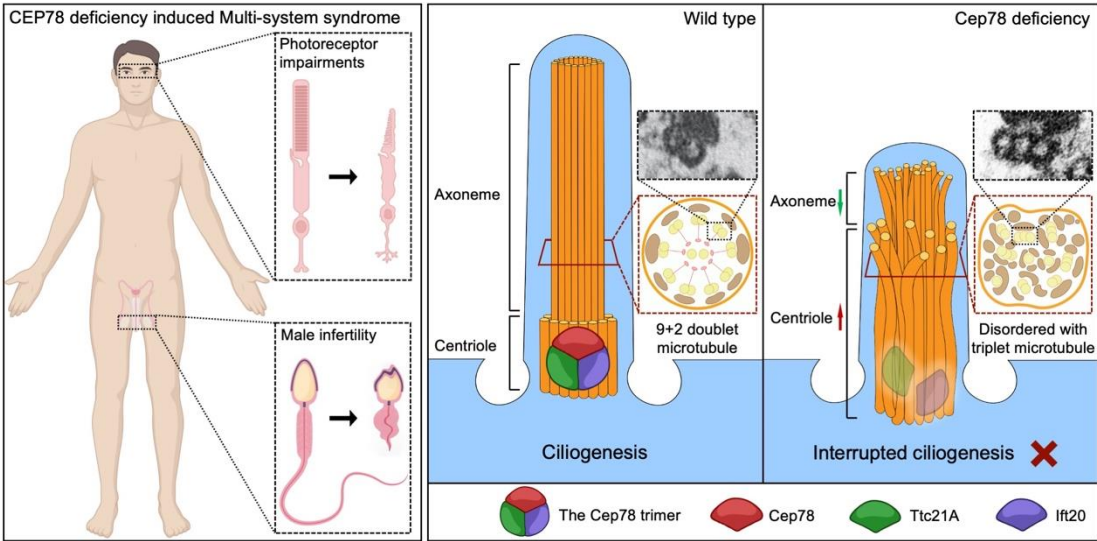
Figure 8. Schematic diagram of pathogenesis induced by Cep78 deficiency. Loss of Cep78 deregulated the expression of and interactions between Ift20 and Ttc21a, two components of the Cep78 trimer. Cep78 deletion causes elongated centrioles, shortened axonemes, abnormal presence of triplet microtubules and disordered 9+2 microtubules.